Reducing Energy Losses at the Organic–anode-buffer Interface of Organic Photovoltaics

Kan Ding[1] and Stephen R. Forrest[1,2,3,*]

[1] *Department of Physics, University of Michigan, Ann Arbor, Michigan 48109, USA*

[2] *Department of Electrical Engineering and Computer Science, University of Michigan, Ann Arbor, Michigan 48109, USA*

[3] *Departments of Material Science and Engineering, University of Michigan, Ann Arbor, Michigan 48109, USA*

(Received 3 October 2019; revised manuscript received 11 January 2020; accepted 28 April 2020; published 19 May 2020)

Understanding the sources of energy loss in organic photovoltaic cells can ultimately lead to increasing their power-conversion efficiency. Here we explore energy losses at the interface between an archetype structure comprising a vacuum-deposited tetraphenyldibenzoperiflanthene/C_{70} bulk-heterojunction active layer and several anode buffer layers (ABLs) using a combination of experimental and computational tools. The composition of the active organic region adjacent to the ABL interface is controlled independently from that in the bulk to determine energy losses that are attributed to charge transfer between the organic active region and the ABL. The open-circuit voltage (V_{OC}) can be varied over a range of 120 meV without affecting the short-circuit current and fill factor by growing an interface layer whose composition ranges from 100% C_{70} to 0% C_{70} in tetraphenyldibenzoperiflanthene at the active-region–ABL interface. Kinetic Monte Carlo simulations are used to quantitatively evaluate the magnitude of the interfacial energy loss and change in V_{OC} with various interface-layer compositions. When the interface layer consists of neat C_{70} that permits nondissipative hole tunneling into the ABL, the interfacial energy loss is reduced and V_{OC} increases by 20–40 mV compared with conventional devices with a homogenous mixed active region.

DOI: 10.1103/PhysRevApplied.13.054046

I. INTRODUCTION

Thin-film organic photovoltaics (OPVs) have drawn considerable attention due to their potential advantages such as flexibility, light weight, semitransparency, and low cost compared with inorganic solar cells [1,2]. With the use of recently developed organic materials and device architectures, the power-conversion efficiency of OPVs now exceeds 16% [3]. However, a comprehensive understanding of photogeneration is still lacking even in the simplest device structures—a process that is complicated by morphological and energetic disorder that leads to charge localization [4,5]. The energy loss, usually defined as the energy difference between the optical gap and the open-circuit voltage, V_{OC}, is a defining feature of OPV performance [6]. Recent studies of energy losses incurred during photogeneration have focused primarily on the role of charge-transfer (CT) states in bulk-heterojunction (BHJ) OPVs [5,7–10]. However, CT states are not the only source of energy loss. In this work, we reveal that energy losses at the interface between the organic BHJ and the anode buffer layer (ABL) can be as large as 0.4 eV. We study an archetype BHJ comprising tetraphenyldibenzoperiflanthene (DBP) as the donor and C_{70} as the acceptor, along with several commonly used ABLs, including MoO_x, poly(3,4-ethylenedioxythiophene)-polystyrene sulfonate (PEDOT-PSS), and 1,4,5,8,9,11-hexaazatriphenylenehexacarbonitrile (HATCN) [11–13]. The energy landscape near the active-region–ABL interface is studied by ultraviolet photoelectron spectroscopy (UPS). We find that for MoO_x and PEDOT-PSS, there is frontier-energy-level bending near the active-region–ABL interface that leads to energy losses [14]. By independently controlling the donor: acceptor ratio of the BHJ near the active-region–ABL interface, we can vary V_{OC} over a range of 120 ± 10 mV independently of the short-circuit current (J_{SC}) and fill factor (FF). Kinetic Monte Carlo simulations are used to quantitatively evaluate the interfacial energy loss by revealing the charge dynamics near the active-region–ABL interface. Insertion of a thin layer of acceptor between the BHJ and certain anode buffer layers is found to reduce the energy loss and increase V_{OC} compared with conventional device architectures.

II. THEORY

We start the investigation by focusing on archetype DBP/C_{70}-based OPVs with a MoO_x ABL and a

*stevefor@umich.edu

bathophenanthroline cathode buffer layer. To study the interface and the bulk properties separately, we insert a thin anode interface layer (AIL) between the BHJ (hereafter referred to as the "bulk layer") and the ABL with various C_{70} concentrations (x) different from that in the bulk layer (y), as shown in Fig. 1(a). MoO_x is a commonly used anode buffer material with a work function of 6.8 eV [13]. Photogenerated holes are extracted through the MoO_x by recombining with electrons injected from the anode [11,15]. It has been reported that because of the high work function of MoO_x, electrons in the highest occupied molecular orbital (HOMO) of the donor transfer into the MoO_x conduction band (CB), pinning its Fermi level to near the organic HOMO [11,15–17]. The electric field from the resulting static interface dipole causes the orbital energies near the interface to bend toward the lower-binding-energy direction, while also broadening the density of states on the organic side of the interface [14,18,19].

Figure 1(b) shows the energy-level diagram of the OPV at open circuit. We assume the hole quasi-Fermi-level E_{Fh} is at δ_1 above the DBP HOMO level on the anode side, E_{DBP}, and the electron quasi-Fermi-level E_{Fe} is at δ_2 below the level of the C_{70} lowest unoccupied molecular orbital (LUMO) on the cathode side, E_{C70}. δ_1 and δ_2 can be either positive or negative depending on the energy alignment at the interfaces. Then E_{DBP} and E_{C70} have following relationship:

$$E_{\mathrm{DBP}} = E_{C_{70}} - \Delta E_{\mathrm{HL}} - qV_a + qV_{\mathrm{int}}, \tag{1}$$

where ΔE_{HL} is the energy offset between the C_{70} LUMO and the DBP HOMO, V_a is the voltage drop across the bulk (active) layer, V_{int} is the voltage drop across the AIL due to the presence of a static interface dipole, and q is the elementary charge. The direction of V_{int} is defined as opposite to V_{a} and the external device voltage, V, by convention. Therefore, V is given by

$$\begin{aligned} qV &= E_{Fe} - E_{Fh} = (E_{C_{70}} - \delta_2) - (E_{\mathrm{DBP}} + \delta_1) \\ &= \Delta E_{\mathrm{HL}} - \delta_2 - \delta_1 + qV_a - qV_{\mathrm{int}}. \end{aligned} \tag{2}$$

Figure 2(a) shows the energy-level diagram near the active-region–ABL interface, with the electron and hole currents represented by blue and yellow arrows, respectively. When forward biased, electrons transfer from the organic HOMO into MoO_x, leaving holes in the organic that flow into the BHJ and recombine with electrons injected from cathode. This is the dark current J_D. Under illumination, a photocurrent, J_{ph}, generated in the active region flows through the ABL interface, where photogenerated holes recombine with electrons in the MoO_x. While J_D depends on both the interface and bulk properties, J_{ph} depends primarily on recombination in the bulk, provided that interface recombination is insignificant. Under open-circuit conditions, $J_D = -J_{\mathrm{ph}}$ and the total current is zero.

Because the BHJ blend morphology is isotropic, photogenerated charges require the guidance of the electric field in the BHJ to reach the electrodes. The direction of J_{ph} is decided by the sign of V_a. Thus, it follows that when $V_a = 0$, then $J_{\mathrm{ph}} = 0$. Assuming the current dependences of δ_1, δ_2, and V_{int} are small, Eq. (2) becomes

$$qV(J_{\mathrm{ph}} = 0) = \Delta E_{\mathrm{HL}} - \delta_2 - \delta_1 - qV_{\mathrm{int}}. \tag{3}$$

Then, using Eqs. (2) and (3), we have

$$V = V(J_{\mathrm{ph}} = 0) + V_a. \tag{4}$$

This scenario suggests that reducing V_{int} may be an effective way to reduce energy losses at the active-region–ABL interface. To achieve this objective, we can eliminate the DBP in the AIL, as shown in Fig. 2(b). The deeper HOMO

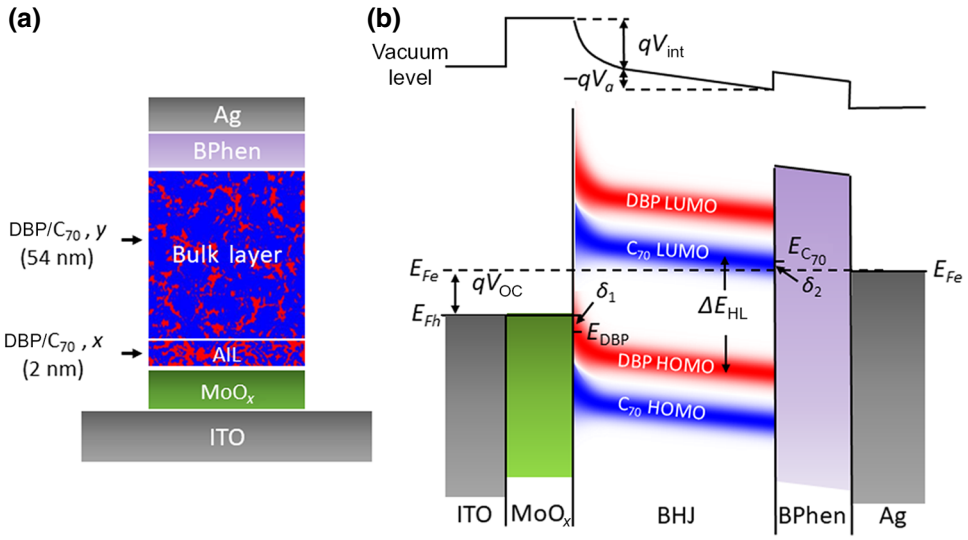

FIG. 1. (a) OPV cell structure with the active region divided into the interface and the bulk regions with C_{70} concentrations of x and y, respectively. (b) Energy-level diagram of a DBP/C_{70} OPV at open circuit. The blurred red and blue lines represent the DBP and C_{70} HOMOs with a finite width of the density of states. BPhen, bathophenanthroline.

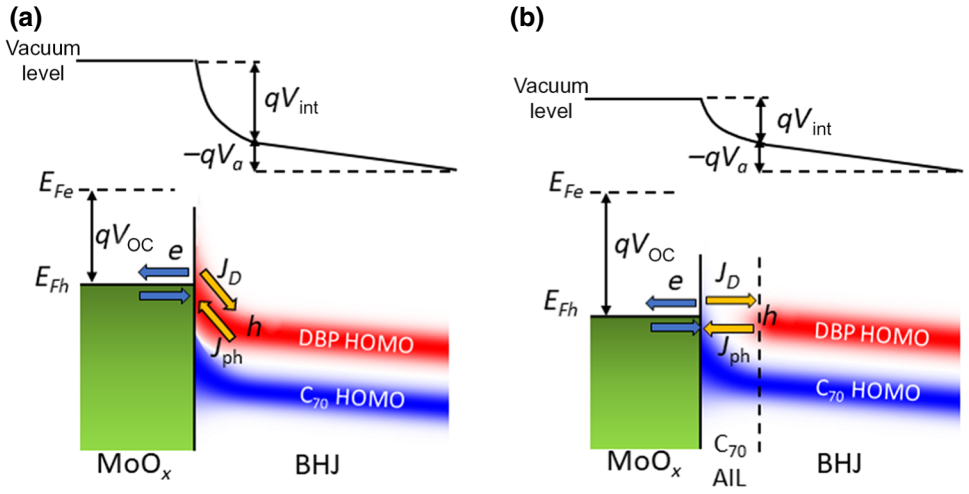

FIG. 2. (a) Energy-level diagram near the interface between a DBP/C_{70} mixed layer and MoO_x at open circuit. The blue and yellow arrows represent the flow of electrons and holes, respectively. (b) Energy-level diagram near the interface between a DBP/C_{70} mixed layer and MoO_x at open circuit when a 2-nm-thick neat C_{70} AIL is inserted between the bulk layer and MoO_x.

of C_{70} pins the Fermi level of MoO_x, resulting in reduced V_{int}. Hole transport between the DBP HOMO in the bulk and the C_{70} HOMO in the AIL is required to extract photogenerated holes [20]. As long as the AIL is thin, this transport can be via tunneling and hence is nondissipative. Therefore, V_{OC} will undergo a rigid shift without a change in V_a and J_{ph}.

III. EXPERIMENT

To test the dependence of energy loss on the properties of the AIL, we fabricate the following devices: indium tin oxide (ITO)/ABL/DBP/C_{70} (x, 2 nm)/DBP/C_{70} (y; 54 nm)/bathophenanthroline (8 nm)/Ag (100 nm), where $x = 0\%$ to 100% and $y = 20\%$ to 90% are the C_{70} concentrations in the interface and bulk layers, respectively [see Fig. 1(a)]. The ITO-coated glass substrates are cleaned by a sequential treatment in 1% Tergitol solution, dionized water, acetone and isopropyl alcohol, and exposed to ultraviolet ozone for 10 min before use. The ABLs studied are MoO_x, PEDOT-PSS, and HATCN. The PEDOT-PSS solution (Clevios P VP AI 4083 from Heraeus) is filtered with a 0.45-μm nylon syringe filter, and the substrate is then spin coated at 6000 revolutions/min for 60 s. The sample is then annealed at 150 °C for 30 min. The thickness of the PEDOT-PSS layer is measured with an ellipsometer to be 40–50 nm. The 10-nm-thick MoO_x and HATCN ABLs are deposited along with the other layers by vacuum thermal evaporation at rates between 0.2 and 1.6 Å/s in a chamber with a base pressure of 10^{-7} Torr. The mixed active layers are codeposited at a rate of 0.2 Å/s for DBP, while the deposition rate for C_{70} is adjusted to achieve the desired volume ratio. The devices are tested in a glovebox filled with ultrapure N_2 (less than 1 ppm O_2 and H_2O) in the dark and under simulated AM1.5G illumination from a calibrated solar simulator at an intensity of 100 mW/cm^2 (1 sun equivalent).

Photoluminescence spectra of the active layers are measured by growing 200-nm-thick thin films on sapphire substrates and exciting them in vacuum by a continuous-wave He-Cd laser with a wavelength of 442 nm. The photoluminescence spectra are collected normal to the substrate with a fiber-coupled monochromator (Princeton Instruments SP-2300i) combined with a Si charge-coupled-device array (PIXIS:400) and an (In,Ga)As photoreceiver (Newport model 2153). The HOMO energies of organic active layers near the active-region–ABL interface are measured by growing organic films of various thicknesses onto the ABL on ITO on glass. Samples are deposited in the same vacuum-thermal-evaporation chamber as the OPVs and the samples for photoluminescence measurements, and are transferred into a vacuum chamber with a base pressure of 10^{-7} Torr. The HOMO energy is measured by UPS with a 21.2-eV ultraviolet photon source at −8.0-V bias.

To determine the electric field and potential drop across the active-region–ABL interface, studies must consider the nanoscale connectivity between donor and acceptor molecules within the BHJ. For this purpose, Monte Carlo simulations provide a suitable method for modeling the discrete paths taken by charges, and electron-transfer processes involving across the AIL, as well as the hole dynamics in the active region [4,21–23]. From this, we obtain the static charge-density distribution near the active-region–ABL interface needed to quantitatively determine the magnitude of the interface dipole and voltage drop, V_{int} (see the Appendix).

IV. RESULTS

Figure 3(a) shows the current-density–voltage (J-V) characteristics of OPVs for MoO_x as the ABL, a bulk-layer C_{70} concentration of $y = 90\%$, and various C_{70} concentrations, x, in the AIL. As x increases, the measured J-V characteristics rigidly shift to higher voltage, as shown

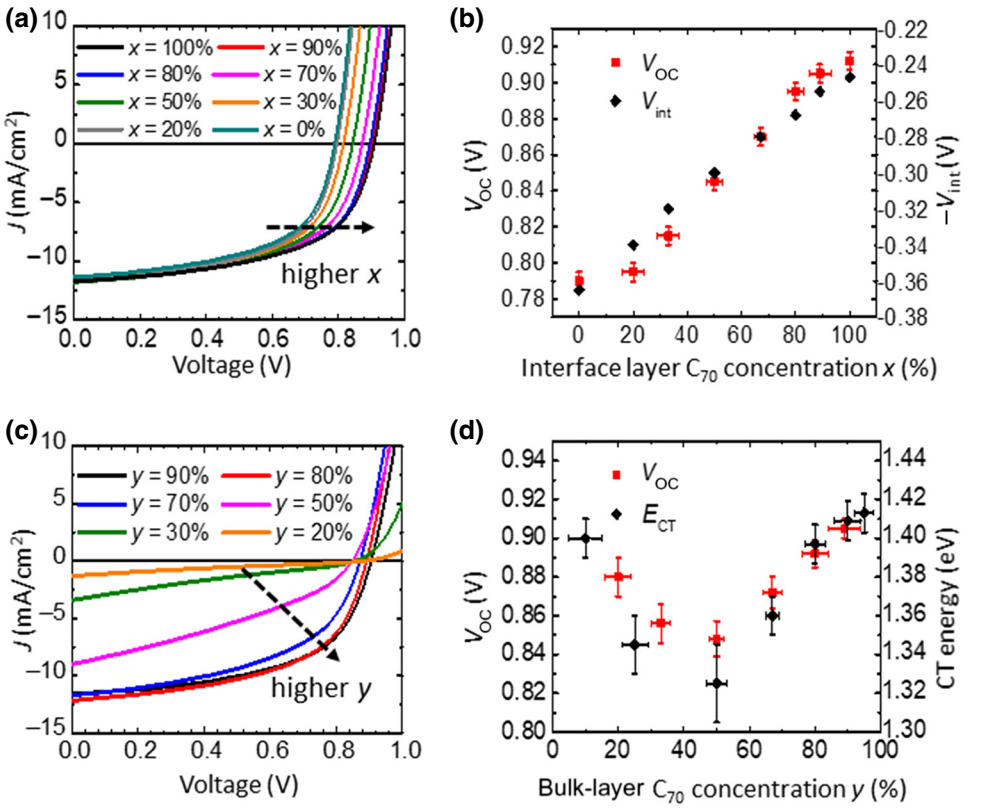

FIG. 3. (a) Current-density–voltage (J-V) characteristics under 1-sun-simulated AM1.5G illumination of OPVs with identical C_{70} concentrations of $y = 90\%$ in the bulk and various C_{70} concentrations, x, in the AIL. (b) Open-circuit voltage, V_{OC} (red squares), and simulated interfacial potential drop, V_{int} (black diamonds), versus x. (c) J-V characteristics of OPVs with $x = 100\%$ and various values of y. (d) Device V_{OC} (red squares) and charge-transfer-state energy measured from photoluminescence spectra (black diamonds) versus y.

in Fig. 3(b) (squares), whereas J_{SC} is nearly unchanged. The V_{OC} difference, ΔV, between devices with a neat C_{70} and a neat DBP AIL is 0.12 ± 0.01 V. The calculated V_{int} at various values of x are also plotted in Fig. 3(b) (diamonds), showing quantitative agreement with measurements.

Figure 3(c) shows the J-V characteristics of devices with constant AIL C_{70} concentration ($x = 100\%$) and various values of y, with V_{OC} shown in Fig. 3(d) (squares) along with CT-state energies acquired from their PL spectra (diamonds) [7]. V_{OC} and the CT exciton energy have similar dependences on y, both showing a minimum near $y = 50\%$, which was previously shown to be due to the minimization of C_{70} or DBP aggregate formation [5,7–9].

To separate the dependences of J_D, J_{ph}, and J on voltage, we calculate J_{ph} by subtracting J_D from the total current, J, and plot the contributions in Fig. 4(a) for devices with either a C_{70} AIL or a DBP AIL. Using Eq. (4), we replot the J-V characteristics in Fig. 4(a) with reference to V_a for each device in Fig. 4(b). Figure 5 shows the J-V characteristics of OPVs with $y = 80\%$ and AILs of various thicknesses. As the AIL thickness increases from 0 to 5 nm, V_{OC} increases, while J_{SC} remains nearly constant. When the AIL is 8 nm thick, however, J_{SC} and

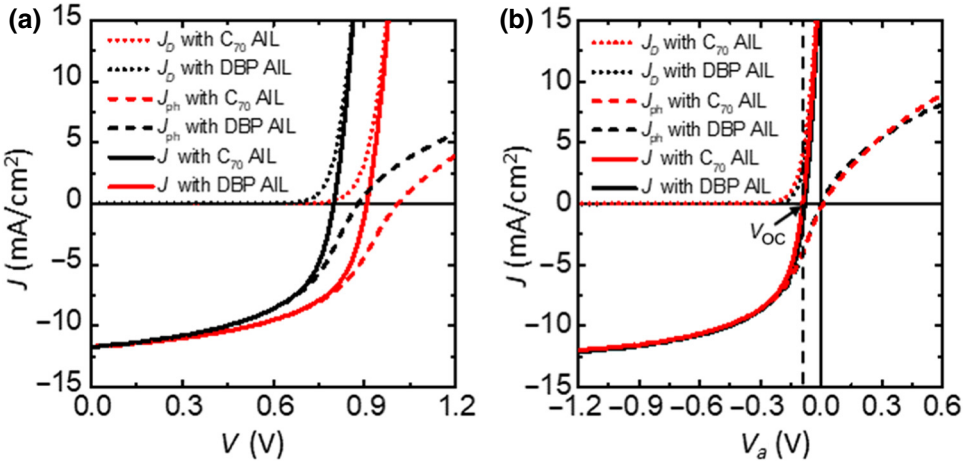

FIG. 4. (a) J-V characteristics for the dark-current density J_D (dotted lines), photocurrent density J_{ph} (dashed lines), and total current density J (solid lines) of devices with a C_{70} AIL (red lines) and a DBP AIL (black lines). (b) The same J-V characteristics as in (a) replotted with reference to voltage across the active layer, V_a. The vertical dashed line corresponds to V_{OC}.

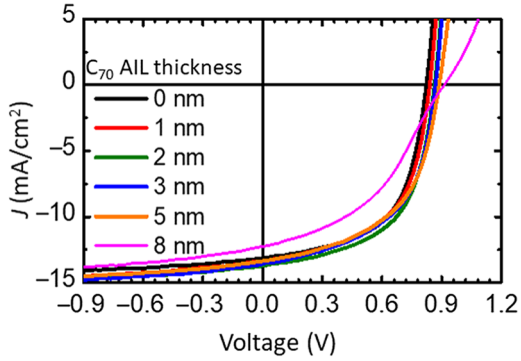

FIG. 5. J-V characteristics of OPVs with a neat C_{70} AIL of various thicknesses. The bulk layer of all devices consists of DBP as a donor and C_{70} as an acceptor with $y = 80\%$.

the FF decrease and the curve exhibits a weak inflection near V_{OC}.

Figure 6(a) shows the illuminated J-V characteristics of OPVs with a C_{70} AIL (solid lines) and a DBP AIL (dashed lines) and $y = 90\%$ (red lines), $y = 50\%$ (blue lines), and $y = 30\%$ (black lines). For $y = 90\%$ and 50%, different AILs exhibit rigid horizontal shifts of their J-V characteristics. The voltage shift $\Delta V = 0.02 \pm 0.01$ V for devices with $y = 50\%$ is smaller than that for devices with $y = 90\%$ ($\Delta V = 0.12 \pm 0.01$ V). For $y = 30\%$, the J-V characteristics show only a weak photoresponse with a high resistance in the forward-biased direction. The simulated results of the hole density ρ_h (histogram) and potential shift from the bulk $\Delta\varphi$ (lines) near the active-region–ABL interface for devices with a C_{70} AIL or a DBP AIL and $y = 90\%$ and 50% are plotted in Figs. 6(b) and 6(c). V_{int} is equal to $\Delta\varphi$ at $z = 0$ nm.

The J-V characteristics of OPVs under illumination with a PEDOT-PSS ABL are shown in Fig. 7(a) with $y = 90\%$ and a C_{70} AIL (black line) or a DBP AIL (red line). The device with a C_{70} AIL shows a larger V_{OC} but a similar J_{SC} and FF as the device with a DBP AIL, which is comparable to the case with a MoO_x ABL. The OPV J-V characteristics with a HATCN ABL are shown in Fig. 7(b) with $y = 90\%$ and a C_{70} AIL (black line) or a DBP AIL (red line). The device with a C_{70} AIL shows a reduced V_{OC} and FF.

The HOMO energies proximal to the ABL interface measured by UPS are shown in Fig. 8. For MoO_x and PEDOT-PSS, there is bending of the organic HOMO energy near the ABL. The energy bending was previously shown to result from a static interface dipole formed by electron transfer from the active region to the MoO_x and PEDOT-PSS [11,15,24–28]. The total bending in the C_{70} HOMO energy is 0.4 ± 0.2 eV for MoO_x and 0.2 ± 0.1 eV for PEDOT-PSS. The energy bending extends over a distance of $\lambda = 30 \pm 10$ Å from the ABL interface. For the C_{70}/HATCN interface, no energy bending is observed.

V. DISCUSSION

The dependence of V_{OC} on the C_{70} concentration in the AIL, x [Fig. 3(b)], and in the bulk, y [Fig 3(d)], reveals the different origins of the energy losses in the two

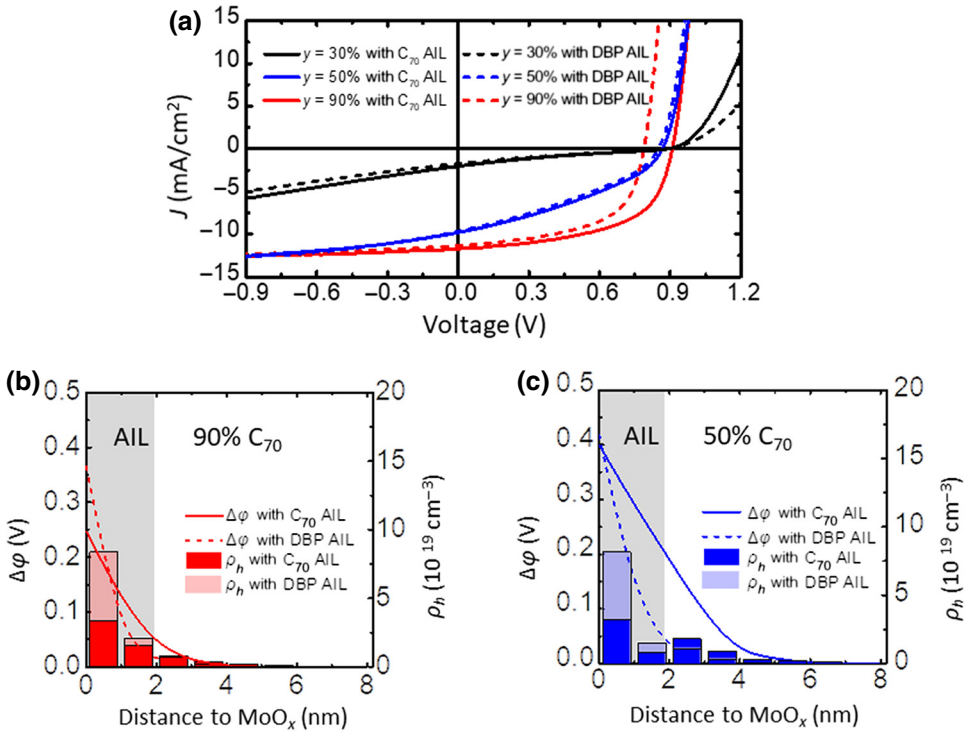

FIG. 6. (a) J-V characteristics of OPVs with $x = 100\%$ (solid lines) and $x = 0\%$ (dashed lines) when $y = 90\%$ (red lines), $y = 50\%$ (blue lines), and $y = 30\%$ (black lines). (b) Simulated hole density ρ_h (histogram) and electric potential shift from the bulk $\Delta\varphi$ (lines) near the active-region–ABL interface for devices with a C_{70} AIL or a DBP AIL with $y = 90\%$. (c) Simulated ρ_h (histogram) and $\Delta\varphi$ (lines) near the active-region–ABL interface for devices with a C_{70} AIL or a DBP AIL with $y = 50\%$.

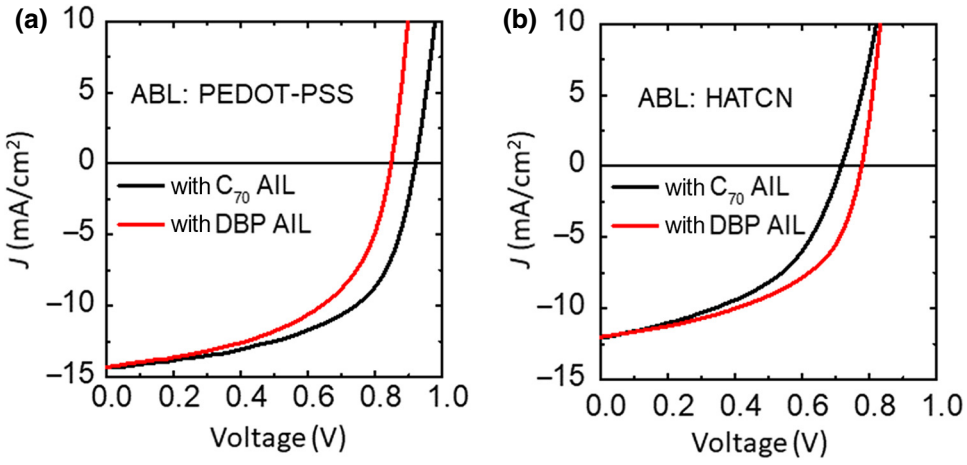

FIG. 7. (a) J-V characteristics of OPVs with PEDOT-PSS as the ABL with a C_{70} AIL (black line) and a DBP AIL (red line) when $y = 90\%$. (b) J-V characteristics of OPVs with HATCN as the ABL with a C_{70} AIL (black line) and a DBP AIL (red line) when $y = 90\%$.

active-region sections. For $y = 90\%$, V_{OC} and the simulated V_{int} show similar monotonic dependences on x [see Fig. 4(b)]. This indicates that the energy loss at the active-region–ABL interface is governed by V_{int} as described in Sec. II. However, the energy loss in the bulk layer is closely related to the CT-state energy in the bulk, as suggested by the similar dependences on y of V_{OC} and CT energy when x is fixed [see Fig. 3(d)].

As shown in Fig. 4(a), both J_D and J_{ph} feature a rigid shift relative to the device voltage, V, depending on the composition of the AIL. As shown in in Fig. 4(b), the J_{ph}-V_a relationships for the two devices are almost identical in the region of $J_{ph} < 0$, showing that photogeneration in the BHJs is indeed governed by V_a and is unaffected by V_{int}, in agreement with the simulations. Both devices show V_{OC} at $V_a = -0.10 \pm 0.01$ V, as denoted by the vertical dashed line. The device with a C_{70} AIL has a slightly higher J_D at a given V_a, which is possibly due to a reduced hole injection barrier [17].

Holes traverse the AIL across thicknesses comparable to the sum of energy-bending-region thickness λ (30 ± 10 Å as shown in Fig. 8) plus the hole tunneling distance through the organic, which can be as large as 4 nm [20]. As shown in Fig. 5, V_{OC} increases with AIL thicknesses less than 5 nm, while J_{SC} remains nearly unaffected. When the AIL thickness is 8 nm, however, it exceeds the tunneling length and thus acts as a hole-blocking layer, leading to distorted J-V characteristics with a reduced J_{SC} and FF. At this point, charges must transfer across the barrier by thermionic emission, which is inherently dissipative. While this may appear as an increase in V_{OC}, it is accompanied by a decrease in J_{ph} and the fill factor, thus reducing the power-conversion efficiency of the solar cell.

Besides the contribution from the AIL, the voltage shift also depends on the C_{70} concentration, y, in the bulk. As y changes from 90% to 50%, ΔV between devices with a C_{70} AIL and a DBP AIL drops from 0.12 ± 0.01 V to 0.02 ± 0.01 V, as shown in Fig. 6(a). When $y = 90\%$, ρ_h near the interface is lower with a C_{70} AIL than with a DBP AIL, leading to a 30% drop in V_{int} (from 0.37 to 0.25 V); see Fig. 6(b). When $y = 50\%$, the device with a C_{70} AIL still has lower ρ_h near the interface, as shown in Fig. 6(c). But because of the higher DBP concentration in the bulk compared with the C_{70} AIL, a portion of the holes diffuse into the bulk, resulting in a larger average electron-hole separation. As a result, V_{int} for devices with a C_{70} AIL or DBP AIL are similar. When the bulk layer has only 30% C_{70}, the device J-V characteristics no longer show a rigid horizontal shift, and the shape changes from that of the devices with thinner AILs (black lines in Fig. 6), suggesting the formation of an energy barrier with impedance to charge extraction [29].

Similar rigid shifts of the J-V characteristics are observed for devices with a PEDOT-PSS ABL with a voltage shift of 0.07 ± 0.01 V, as shown in Fig. 7(a).

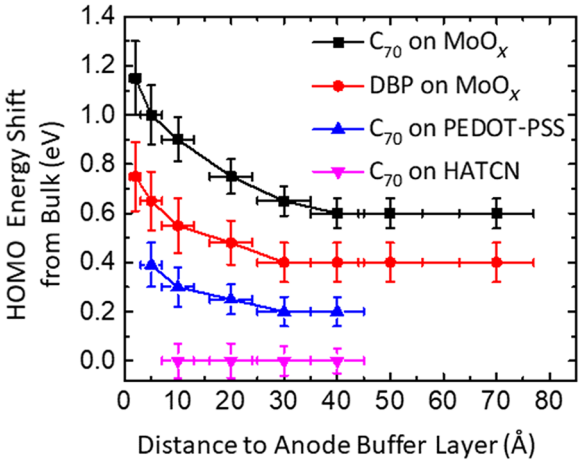

FIG. 8. HOMO energy bending (relative to the bulk) versus distance from the ABL interface for the C_{70}/MoO_x interface (black), DBP/MoO_x interface (red), C_{70}/PEDOT-PSS interface (blue), and C_{70}/HATCN interface (pink) measured by ultraviolet photoelectron spectroscopy. The vertical error bars represent the energy resolution of the measurement and the horizontal error bars represent the uncertainty of the organic layer thickness.

TABLE I. Device performance with various active layers with and without an acceptor AIL.

Device active layer	J_{SC} (mA/cm^2)	V_{OC} (V)[b]	FF[b]	PCE[c] (%)
DBP/C_{70} (1:4, 60 nm)	12.6 ± 0.2	0.86	0.54	5.8 ± 0.1
DBP/C_{70} (1:4, 60 nm)[a]	12.6 ± 0.2	0.88	0.54	6.0 ± 0.1
DTDCPB/C_{70} (1:2, 80 nm)	13.9 ± 0.2	0.90	0.70	9.2 ± 0.2
DTDCPB/C_{70} (1:2, 80 nm)[a]	14.1 ± 0.2	0.94	0.71	9.8 ± 0.2
DTDCTB/C_{60} (1:3, 80 nm)	10.4 ± 0.3	0.80	0.47	3.9 ± 0.2
DTDCTB/C_{60} (1:3, 80 nm)[a]	10.6 ± 0.3	0.84	0.46	4.1 ± 0.2

[a]Device has a 3-nm-thick acceptor AIL.
[b]Errors are ± 0.01.
[c]*PCE*, power-conversion efficiency.

This agrees with the energy bending observed at the C_{70}/PEDOT-PSS interface in Fig. 8. No energy bending is observed at the C_{70}/HATCN interface. As a result, the AIL causes a drop in V_{OC} and the FF, as shown in Fig. 7(b). This suggests that the energy bending at the interface is responsible for hole transport across the AIL.

Apart from DBP/C_{70}, we also test the effect of an acceptor AIL on two other donor-acceptor systems: 2-[(7-[4-[*N*,*N*-bis(4-methylphenyl)amino]phenyl]-2,1,3-benzothiadiazol-4-yl)methylene] propanedinitrile (DTDCPB)/C_{70} and 2-[[7-(5-*N*,*N*-ditolylaminothiophen-2-yl)-2,1,3-benzothiadiazol-4-yl]methylene]malononitrile (DTDCTB)/C_{60}. Table I shows device characteristics of the three donor-acceptor material systems with and without the acceptor AIL. All three systems show increases in V_{OC} and power-conversion efficiency with an acceptor AIL.

VI. CONCLUSIONS

In this study, we show that a static dipole at the active-region–ABL interface introduces energy loss. By removing the donors near the active-region–ABL interface, we can reduce the loss by up to 30%. A change in interfacial energy loss results in a concomitant change in V_{OC}, while J_{SC} and the FF remain unaffected. V_{OC} can be controlled over a range of 120 ± 10 meV by varying the donor:acceptor ratio near the interface. We attribute the change in V_{OC} to the change in the potential drop across the interface dipole layer at various interfacial donor:acceptor ratios, which is supported by Monte Carlo simulations. A significant outcome of our work is the demonstration of a counterintuitive but effective strategy to reduce the energy loss by inserting a thin electron-accepting layer between the active region and the anode buffer. A primary condition for this layer is that it must be sufficiently thin to support nondissipative charge tunneling, resulting in an increase in V_{OC} without a decrease in the current or fill factor.

This work illuminates the different roles played by the interface and bulk layers in the photogeneration process, showing that their compositions should be independently controlled to optimize OPV performance. It also demonstrates that acceptors can transport holes and reduce the energy loss for hole extraction in OPVs with the help of an interface dipole layer.

ACKNOWLEDGMENTS

We gratefully thank Dr. Shaocong Hou, Dr. Xiao Liu, Dr. Yongxi Li, Dr. Quinn Burlingame, Dr. Caleb Coburn, Yue Qu, Xinjing Huang, Jongchan Kim, and Byungjun Lee for helpful discussions. This work was partially supported by the Department of the Navy, Office of Naval Research, under Grant No. N00014-17-1-2211 (K.D., simulations, experiment, and analysis; S.R.F., analysis) and Universal Display Corporation.

APPENDIX: MONTE CARLO SIMULATIONS

We use kinetic Monte Carlo simulations to determine the charge distribution near the organic/MoO_x interface as a means for estimating V_{int}. For $y > 50\%$, V_{int} has a weak dependence on J as shown in Fig. 6(a). Thus, we need only to calculate V_{int} at open circuit ($J = 0$) to describe the rigid shift in the J-V characteristics. Three charge-transfer processes are considered in the simulation: electron transfer from the organic to the MoO_x layer, recombination of electrons in MoO_x with holes in the organic, and hole diffusion in the organic. The simulation consists of a $100 \times 100 \times 10$ nm^3 organic layer where the molecules form a simple cubic lattice with a lattice constant of 1 nm. The frontier orbital energies of the organics are assumed to be accurately described by a Gaussian distribution with a standard deviation of 0.1 eV [4,30]. Initially, both the MoO_x layer and organic layer are neutral. As the simulation proceeds, electrons transfer from the HOMOs of both the donor and the acceptor to the MoO_x CB due to its high work function (6.7 eV), leaving behind holes in the organic layer [30–33]. The charge-transfer rate from organic molecules to MoO_x is assumed to follow Miller-Abrahams hopping:

$$P = P_0 \exp\left(-\frac{E_F - E_i}{kT}\right), \quad E_F > E_i, \qquad P = P_0, \quad E_F < E_i, \tag{A1}$$

where E_F is the MoO_x Fermi level, E_i is the HOMO energy of molecule i, P_0 is the maximum hopping rate, which is proportional to the overlap between the electron wave functions in the organic and MoO_x, k is the Boltzmann constant, and T is the temperature.

Electrons in the MoO_x CB can also transfer back into the organic by recombining with holes near the interface. The recombination rate is also calculated with Eq. (A1), with E_F and E_i swapped. Thermal equilibrium is reached when electron transfer is balanced by electron-hole recombination across the interface. The holes in the organic layer can also diffuse among neighboring molecules. For either the recombination event or the diffusion event to happen, there is a wait time:

$$\tau = -\frac{\ln X}{P}, \tag{A2}$$

where X is a random number between 0 and 1. The transfer event with the smallest wait time τ happens first. After each event, the energy of every organic site is updated on the basis of the electric field from the charges with use of the following equation:

$$E_i = E_{i0} - \int_{z_0}^{z_i} F(z)dz, \tag{A3}$$

where E_{i0} is the HOMO energy when $F=0$, z_i is the distance of molecule i perpendicular to the interface, z_0 is the z coordinate for a molecule in the bulk (taken at 10 nm from the interface), and $F(z)$ is the electric field. The electric field from the holes is given by

$$\mathbf{F}_{\text{hole}}(\mathbf{r}_i) = \sum_j \frac{q}{4\pi\varepsilon_0\varepsilon_r|\mathbf{r}_i - \mathbf{r}_j|^2}\hat{\mathbf{r}}_{ij}, \tag{A4}$$

where $\mathbf{r}_i$ is the coordinate of site i, $\mathbf{r}_j$ is the coordinate of a hole at j, $\hat{\mathbf{r}}_{ij}$ is the unit vector between the hole and $\mathbf{r}_i$, ε_0 is the vacuum permittivity, and ε_r is the dielectric constant of the organic. To reduce the computational workload, we set a cutoff radius of 4 nm for calculation of the electric field from holes. $F_{\text{hole}}(z)$ is calculated by our taking the average of $\mathbf{F}_{\text{hole}}(\mathbf{r}_i)$ over all sites in a certain plane.

Because of the high conductivity ($\sigma\sim10^{-2}$ S/m) [34] and static dielectric constant ($\varepsilon_r\sim18$) [35] of MoO_x compared with the organic blend (e.g., $\sigma\sim10^{-6}$ S/m [36] and $\varepsilon_r\sim4$ [37] for C_{70}), we consider all the transferred electrons to be uniformly distributed at the MoO_x surface [38,39]. The electric field on the organic side is thus a constant

$$F_{\text{electron}}(z) = \frac{\sigma}{2\varepsilon_0\varepsilon_r}, \tag{A5}$$

where σ is the electron surface density. Because of energetic disorder in the organic thin film, holes diffuse among molecules and distribute themselves across a few interfacial molecular layers. The asymmetric distribution of electrons and holes results in an interface dipole and hence the energy-level shift observed in Fig. 8. The electric potential φ in Figs. 6(b) and 6(c) is calculated by

$$\varphi(z_i) = \int_{z_{\text{bulk}}}^{z_i} F(z)dz, \tag{A6}$$

where $z_{\text{bulk}}=10$ nm by our assuming the electric field at 10 nm is zero.

Hole diffusion is also simulated with use of Eq. (A1), where P_0 is now proportional to the overlap between the HOMOs of two neighboring molecules. Although the absolute values of P_0 have no effect on the simulation results, the ratio of the P_0 values for the two processes matters. We introduce the parameter $\alpha = P_{0\text{diff}}/P_{0\text{trans}}$, where $P_{0\text{diff}}$ is the maximum hopping rate for hole diffusion among organic molecules and $P_{0\text{trans}}$ is the maximum hopping rate for charge transfer between the MoO_x layer and the organic layer. V_{int} in Figs. 6(b) and 6(c) is calculated with $\alpha = 130$. The large value of α is due to the smaller overlap between the organic HOMOs and the electron wave functions in the MoO_x CB compared with the overlap between organic HOMOs.

[1] Y. Lin, Y. Li, and X. Zhan, Small molecule semiconductors for high-efficiency organic photovoltaics, Chem. Soc. Rev. **41**, 4245 (2012).

[2] A. Mishra and P. Bäuerle, Small molecule organic semiconductors on the move: Promises for future solar energy technology, Angew. Chem. Int. Ed. **51**, 2020 (2012).

[3] Y. Cui, H. Yao, J. Zhang, T. Zhang, Y. Wang, L. Hong, K. Xian, B. Xu, S. Zhang, J. Peng, Z. Wei, F. Gao, and J. Hou, Over 16% efficiency organic photovoltaic cells enabled by a chlorinated acceptor with increased open-circuit voltages, Nat. Commun. **10**, 2515 (2019).

[4] H. Bässler, Charge transport in disordered organic photoconductors a monte carlo simulation study, Phys. Status Solidi **175**, 15 (1993).

[5] Y. L. Lin, M. A. Fusella, and B. P. Rand, The impact of local morphology on organic donor/acceptor charge transfer states, Adv. Energy Mater. **8**, 1702816 (2018).

[6] T. Linderl, T. Zechel, M. Brendel, D. Moseguí González, P. Müller-Buschbaum, J. Pflaum, and W. Brütting, Energy losses in small-molecule organic photovoltaics, Adv. Energy Mater. **7**, 1700237 (2017).

[7] X. Liu, K. Ding, A. Panda, and S. R. Forrest, Charge transfer states in dilute donor–acceptor blend organic heterojunctions, ACS Nano **10**, 7619 (2016).

[8] K. Ding, X. Liu, and S. R. Forrest, Charge transfer and collection in dilute organic donor–acceptor heterojunction blends, Nano Lett. **18**, 3180 (2018).

[9] Z. Guan, H.-W. Li, Y. Cheng, Q. Yang, M.-F. Lo, T.-W. Ng, S.-W. Tsang, and C.-S. Lee, Charge-transfer state energy

and its relationship with open-circuit voltage in an organic photovoltaic device, J. Phys. Chem. C **120**, 14059 (2016).
[10] X. Liu, B. P. Rand, and S. R. Forrest, Engineering charge-transfer states for efficient, low-energy-loss organic photovoltaics, Trends Chem **1**, 815 (2019).
[11] J. Meyer, S. Hamwi, M. Kröger, W. Kowalsky, T. Riedl, and A. Kahn, Transition metal oxides for organic electronics: Energetics, device physics and applications, Adv. Mater. **24**, 5408 (2012).
[12] D. Y. Kim, J. Subbiah, G. Sarasqueta, F. So, H. Ding, Irfan, and Y. Gao, The effect of molybdenum oxide interlayer on organic photovoltaic cells, Appl. Phys. Lett. **95**, 093304 (2009).
[13] M. Kröger, S. Hamwi, J. Meyer, T. Riedl, W. Kowalsky, and A. Kahn, Role of the deep-lying electronic states of moo3 in the enhancement of hole-injection in organic thin films, Appl. Phys. Lett. **95**, 123301 (2009).
[14] M. Oehzelt, N. Koch, and G. Heimel, Organic semiconductor density of states controls the energy level alignment at electrode interfaces, Nat. Commun. **5**, 4174 (2014).
[15] C. Wang, I. Irfan, X. Liu, and Y. Gao, Role of molybdenum oxide for organic electronics: Surface analytical studies, J. Vac. Sci. Technol. **32**, 040801 (2014).
[16] J. Wang, L. Xu, Y.-J. Lee, M. De Anda Villa, A. V. Malko, and J. W. P. Hsu, Effects of contact-induced doping on the behaviors of organic photovoltaic devices, Nano Lett. **15**, 7627 (2015).
[17] N. B. Kotadiya, H. Lu, A. Mondal, Y. Ie, D. Andrienko, P. W. M. Blom, and G.-J. A. H. Wetzelaer, Universal strategy for ohmic hole injection into organic semiconductors with high ionization energies, Nat. Mater. **17**, 329 (2018).
[18] M. A. Baldo and S. R. Forrest, Interface-limited injection in amorphous organic semiconductors, Phys. Rev. B **64**, 085201 (2001).
[19] B. N. Limketkai and M. A. Baldo, Charge injection into cathode-doped amorphous organic semiconductors, Phys. Rev. B **71**, 085207 (2005).
[20] A. Melianas, V. Pranculis, D. Spoltore, J. Benduhn, O. Inganäs, V. Gulbinas, K. Vandewal, and M. Kemerink, Charge transport in pure and mixed phases in organic solar cells, Adv. Energy Mater. **7**, 1700888 (2017).
[21] P. K. Watkins, A. B. Walker, and G. L. B. Verschoor, Dynamical monte carlo modelling of organic solar cells: The dependence of internal quantum efficiency on morphology, Nano Lett. **5**, 1814 (2005).
[22] U. Wolf, V. I. Arkhipov, and H. Bässler, Current injection from a metal to a disordered hopping system. I. Monte carlo simulation, Phys. Rev. B **59**, 7507 (1999).
[23] Y. N. Gartstein and E. M. Conwell, Field-dependent thermal injection into a disordered molecular insulator, Chem. Phys. Lett. **255**, 93 (1996).
[24] J.-P. Yang, W.-Q. Wang, L.-W. Cheng, Y.-Q. Li, J.-X. Tang, S. Kera, N. Ueno, and X.-h. Zeng, Mechanism for doping induced p type c60using thermally evaporated molybdenum trioxide (moo3) as a dopant, J. Phys. Condens. Matter **28**, 185502 (2016).
[25] Irfan, M. Zhang, H. Ding, C. W. Tang, and Y. Gao, Strong interface p-doping and band bending in c60 on moox, Org. Electron. **12**, 1588 (2011).
[26] J. Yoo, K. Jung, J. Jeong, G. Hyun, H. Lee, and Y. Yi, Energy level alignment at c60/dtdctb/pedot:Pss interfaces in organic photovoltaics, Appl. Surf. Sci. **402**, 41 (2017).
[27] K. Sotthewes, R. van Bremen, E. Dollekamp, T. Boulogne, K. Nowakowski, D. Kas, H. J. W. Zandvliet, and P. Bampoulis, Universal Fermi-level pinning in transition-metal dichalcogenides, J. Phys. Chem. C **123**, 5411 (2019).
[28] M. T. Greiner, M. G. Helander, W.-M. Tang, Z.-B. Wang, J. Qiu, and Z.-H. Lu, Universal energy-level alignment of molecules on metal oxides, Nat. Mater. **11**, 76 (2011).
[29] W. Tress, in *Organic Solar Cells: Theory, Experiment, and Device Simulation*, edited by W. Tress (Springer International Publishing, Cham, 2014), pp. 315.
[30] J. Yun, W. Jang, T. Lee, Y. Lee, and A. Soon, Aligning the Band Structures of Polymorphic Molybdenum Oxides and Organic Emitters in Light-Emitting Diodes, Phys. Rev. Appl. **7**, 024025 (2017).
[31] Y. Guo and J. Robertson, Origin of the high work function and high conductivity of moo3, Appl. Phys. Lett. **105**, 222110 (2014).
[32] K. Inzani, T. Grande, F. Vullum-Bruer, and S. M. Selbach, A van der waals density functional study of moo3 and its oxygen vacancies, J. Phys. Chem. C **120**, 8959 (2016).
[33] D. O. Scanlon, G. W. Watson, D. J. Payne, G. R. Atkinson, R. G. Egdell, and D. S. L. Law, Theoretical and experimental study of the electronic structures of moo3 and moo2, J. Phys. Chem. C **114**, 4636 (2010).
[34] S. Krishnakumar and C. S. Menon, Electrical and optical properties of molybdenum trioxide thin films, Bull. Mater. Sci. **16**, 187 (1993).
[35] S. K. Deb and J. A. Chopoorian, Optical properties and color-center formation in thin films of molybdenum trioxide, J. Appl. Phys. **37**, 4818 (1966).
[36] L. Firlej, A. Zahab, F. Brocard, and P. Bernier, Electric conductivity in c70 thin films, Synth. Met. **70**, 1373 (1995).
[37] S. L. Ren, K. A. Wang, P. Zhou, Y. Wang, A. M. Rao, M. S. Meier, J. P. Selegue, and P. C. Eklund, Dielectric function of solid c70 films, Appl. Phys. Lett. **61**, 124 (1992).
[38] C. Battaglia, X. Yin, M. Zheng, I. D. Sharp, T. Chen, S. McDonnell, A. Azcatl, C. Carraro, B. Ma, R. Maboudian, R. M. Wallace, and A. Javey, Hole selective moox contact for silicon solar cells, Nano Lett. **14**, 967 (2014).
[39] H. Ding, H. Lin, B. Sadigh, F. Zhou, V. Ozoliņš, and M. Asta, Computational investigation of electron small polarons in α-moo3, J. Phys. Chem. C **118**, 15565 (2014).